Manuscript

Click here to view linked References

The role of MnO_x in Cu-MnO_x/SiO_2 catalysts for the gas-phase hydrogenation of furfural

A.C. Alba-Rubio [1,a], J.A. Cecilia [2,*], C.P. Jiménez-Gómez [2], C. García-Sancho [2], A. Cassidy [1], R. Moreno-Tost [2] and P. Maireles-Torres [2]

[1] University of Toledo, Department of Chemical Engineering, Toledo, OH 43606, USA.

[2] Universidad de Málaga, Departamento de Química Inorgánica, Cristalografía y Mineralogía (Unidad Aso-ciada al ICP-CSIC), Facultad de Ciencias, Campus de Teatinos, Málaga, 29071, Spain.

[a] Current affiliation: Clemson University, Department of Chemical and Biomolecular Engineering, Clemson, SC 29634, USA.

[*]Corresponding autor: jacecilia@uma.es

Abstract

A series of Cu-MnO_x/SiO_2 catalysts was synthesized using different methodologies: incipient wetness impregnation and strong electrostatic adsorption for the incorporation of Cu species and incipient wetness impregnation and controlled surface reactions for the addition of MnO_x. The materials were characterized by H_2-TPR, XRD, XPS, TEM/EDX, and N_2 adsorption-desorption at -196 ºC to study the interaction between Cu and MnO_x species. These catalysts were evaluated in the gas-phase hydrogenation of furfural at 190 ºC. While a highly dispersed Cu/SiO_2 catalyst promoted the hydrogenolysis of furfuryl alcohol to methyl furan, it was found that the presence of oxygen vacancies in MnO_x facilitated the interaction of the catalysts with the carbonyl group of furfural, thus promoting the formation of furfuryl alcohol as the main product.

Keywords

furfural; hydrogenation; copper; manganese; furfuryl alcohol; 2-methylfuran

1. Introduction

The growing world energy demand and the decline of oil reserves, combined with concerns associated with global climate change and pollution, are prompting governments to promote the development of sustainable technologies for the production of fuels and chemicals from non-fossil carbon sources [1,2]. Several energy resources have been suggested in order to reduce the consumption of fossil fuels, but biomass is the only one suitable to produce energy and chemicals without economic, environmental, and social impacts [3,4].

In order to avoid interfering with the food chain, the type of biomass must be carefully selected. In this context, lignocellulosic biomass is a very promising feedstock, since it could be considered a non-edible source and, moreover, it is the most abundant with high availability ($2 \cdot 10^{11}$ metric tons per year) [5–7]. Lignocellulosic biomass is mainly formed by cellulose (40–50%), lignin (15–25%), and hemicellulose (20–35%), requiring previous fractionation before proceeding to its valorization [7]. In particular, hemicellulose consists of pentosans, mainly xylans, which can be subsequently dehydrated to produce furfural (FUR) [8].

FUR is one of the top commercial building blocks produced at lignocellulose-based biorefineries because it can be used for a broad spectrum of industrial applications. Among them, it can be highlighted its use in resin and plastic production, the pharmaceutical industry, and for the extraction of lubricants [1]. In addition, its chemical functionalities (α,β-unsaturated aldehyde with C=O and C=C bonds) provide it with high reactivity, which allows the synthesis of a wide variety of high value-added chemicals, such as furfuryl alcohol (FOL), 2-methylfuran (MF), furan (F), 2-methyltetrahydrofuran (2-MTHF), linear alkanes (pentane or butane), furoic acid, and maleic acid, among others [2,9,10].

Currently, the main product obtained from FUR is FOL, accounting for approximately 65% of furfural production [11]. FOL is an important feedstock for the manufacture of foundry resins, as well as for biofuel production and the synthesis of agrochemicals and bioproducts [1,2,12]. On the other hand, MF and 2-MTHF are promising additives to increase the octane number of gasoline, thus increasing its anti-explosion performance [13,14]. MF can also be used as an intermediate in the

pharmaceutical industry and a precursor for the production of furan-based compounds and pentanediol, among others [15].

FOL and MF are obtained from the hydrogenation of FUR, which can be carried out in gas or liquid phase, although the former does not require high hydrogen pressure, thus reducing the process cost. Currently, copper chromite is the commercial catalyst employed to produce FOL and MF from FUR, but the main disadvantage of this catalyst is the presence of toxic chromium [16,17]. Palladium-based catalysts have also been proposed for FUR hydrogenation, but their high cost and low availability limit their application in large-scale processes [2]. In this context, much research effort is being paid to the search for chromium-free catalysts with high activity, selectivity, and stability, since the nature of the catalyst used, together with the experimental conditions, are key factors in obtaining the highest yield of the desired product [18].

From the last century, several noble and transition metal-based catalysts (Pt, Ru, Pd, Au, Ni, Cu) have been developed for the gas-phase FUR hydrogenation [19–23]. Most of them have been supported in metal oxides (e.g., zinc oxide, magnesium oxide, silica, cerium oxide, or titanium oxide) or carbon to provide highly active and stable catalytic systems associated with the modification of the acidity and basicity of the catalysts [18,22,24–26]. Copper-containing catalysts have demonstrated to be active in the gas-phase FUR hydrogenation due to their excellent interaction with the carbonyl group of the FUR molecule, preventing the scission of the C-C bond and favoring the formation of FOL and MF [27]. In order to enhance the dispersion of copper oxide and increase the number of available active sites, copper has been supported on different oxides by diverse synthetic methods [28,29]. For example, in 1948, Burnette et al. studied the production of MF from the hydrogenation of furfural in the gas phase using supported copper catalysts, since the metal-support interaction affects the activity and stability of the materials [30]. In this case, the highest MF yield was obtained with the Cu-Cr catalyst (above 90 %), while the lowest was reached with a Cu-MnO_x-based catalyst supported on charcoal, being this 21% MF yield. In the last years, several Cu-based catalysts, such as Cu/ZnO [31–34], Cu/SiO_2 [19,32,35], Cu/CeO_2 [18,33], and Cu/MgO [26,36], have shown to be active in FUR hydrogenation, although they were prone to suffer from deactivation, especially when the reactions were carried out in gas phase [16]. In addition, the selectivity pattern depended on the acidic properties of the catalyst, as the activity is mainly affected by the metal-support interaction.Among these supports, Sitthisa et al.

studied the catalytic activity of Cu, Pd, and Ni supported on SiO_2 for furfural hydrogenation at 230 ºC under 0.1 MPa H_2 [19]. During this study, catalysts provided furfural conversion values above 75%. While the incorporation of Pd gave rise to different products, such as furan (60%), THF (20%), and FOL (14%), the Ni-based catalyst favored the opening of the furan ring and generated products by hydrogenation and decarbonylation, such as butane, butanal, and butanol. However, the Cu catalyst showed a more selective hydrogenation to FOL (98%), which makes Cu the preferred metal for the selective hydrogenation of FUR in gas phase. On the other hand, Dong et al. studied the effect of different supports on the catalytic activity by supporting copper on SiO_2, Al_2O_3, and ZnO by precipitation, obtaining the best catalytic performance with the Cu/SiO_2 catalyst (89.5% MF yield at 220 ºC) [32]. In another example, Nagaraja et al. synthesized Cu/MgO catalysts by three different methods: co-precipitation, impregnation, and solid-solid wetting [36]. The best results were obtained with the catalyst prepared by co-precipitation, which showed values of FUR conversion and FOL selectivity of 98% due to the smallest Cu particle size (thus largest Cu dispersion) and the highest BET surface area. Therefore, it has been demonstrated that the synthesis method selected for the introduction of the copper species is crucial for obtaining highly active and stable catalysts. Additionally, it has been studied the use of a second metal to enhance the catalytic performance. For example, Hu el al. added Mn to Cu catalysts, and demonstrated that the reduction of Mn^{3+} to Mn^{2+}, together with well-dispersed Cu nanoparticles, created surface oxygen vacancies that form a Mn^{2+}-O_v-Mn^{2+} defect structure, which is beneficial for the hydrogenation of FUR because those vacancies promote the interaction with the carbonyl group of FUR [37].

In the present work, a series of manganese oxide (MnO_x)-promoted Cu-based catalysts was synthesized and evaluated in the gas-phase hydrogenation of furfural. Due to the important role that the synthesis method plays in the physical-chemical properties of the catalysts, MnO_x was incorporated following three different approaches: incipient wetness impregnation, strong electrostatic adsorption (SEA) [29], and controlled surface reactions (CSR) [38] to evaluate the dispersion of the Cu and MnO_x particles on the catalyst. Moreover, the Cu/Mn atomic ratio and the reaction conditions were optimized to attain the highest values of conversion while evaluating the selectivity pattern towards hydrogenated products, such as FOL or MF. Furthermore, $Cu\text{-}MnO_x/SiO_2$ catalysts were compared with Cu/SiO_2 to evaluate the influence of the MnO_x species in the catalytic

behavior. All catalysts were also characterized by different techniques to determinate their physical-chemical properties and understand the interaction between both metals as a function of the synthesis method, the metal-support interaction, and the catalytic activity in the FUR hydrogenation.

2. Materials and Methods

2.1. Reagents and Materials

A commercial CAB-O-SIL® EH-5 fumed silica provided by Cabot Corporation was utilized as the support. The following chemicals were used for the synthesis of catalysts: $Cu(NH_3)_4SO_4{\cdot}H_2O$ (Sigma-Aldrich, 99%), $Cu(NO_3)_2{\cdot}3H_2O$ (VWR, 99%), $Mn(NO_3)_2{\cdot}4H_2O$ (Sigma-Aldrich, 99%), $C_5H_5Mn(CO)_3$ (Sigma-Aldrich, 99%), and anhydrous tetrahydrofuran (Sigma-Aldrich, ≥99.9%, inhibitor-free). On the other hand, furfural (FUR) (Sigma-Aldrich, 99%) and cyclopentylmethyl ether (CPME) (Sigma-Aldrich, 99.9%) were employed in the FUR hydrogenation. Likewise, different gases were utilized: He (Air Liquide, 99.99%), H_2 (Air Liquide 99.999%), N_2 (Air Liquide, 99.9999%), Ar (Airgas, 99.999%), H_2/Ar (10% vol. H_2, Air Liquide), N_2O/He (35% vol. N_2O, Air Liquide), and O_2/N_2 (0.5 vol.% O_2, Airgas).

2.2. Synthesis of Catalysts

Firstly, a monometallic Cu/SiO_2 catalyst was synthesized by strong electrostatic adsorption (SEA) [39]. To do so, 4 g of silica was put in contact with 1 L of deionized water under stirring. Next, a $Cu(NH_3)_4SO_4{\cdot}H_2O$ solution in water was added to obtain a final copper loading of 15 wt.%. Then, the pH of this solution was adjusted to 9 by using very diluted NH_4OH and H_2SO_4 solutions, and stirring was maintained for 20 h. After that, the solution was filtered and washed with deionized water, thus obtaining the catalyst precursor. After reduction, which will be described later, this catalyst was labeled as Cu_{SEA} to indicate its monometallic nature and the method used to support the copper species.

Regarding the MnO_x-promoted catalysts, different synthesis methods were selected in order to study the interaction between Cu and MnO_x species: incipient wetness impregnation (IMP), strong electrostatic adsorption (SEA), and controlled surface reactions (CSR). In all cases, commercial SiO_2 was used as the support and a 15 wt% Cu loading was selected, while varying the Mn concentration to obtain Mn:Cu atomic ratios equal to 0.15, 0.30, and 0.45. These catalysts were labeled as $1Cu_x{:}zMn_y$ where *x* and *y*

indicate the method used to incorporate Cu and Mn, respectively, and *z* is the Mn/Cu atomic ratio.

First, catalysts synthesized by incipient wetness impregnation were prepared by putting in contact silica with an aqueous solution containing appropriate amounts of $Cu(NO_3)_2{\cdot}3H_2O$ and $Mn(NO_3)_2{\cdot}4H_2O$ salts.

Another series of catalysts was prepared by incorporating 15 wt% Cu by the SEA method, as previously described for the Cu_{SEA} catalyst precursor, and without reduction, further addition of Mn species by incipient wetness impregnation using $Mn(NO_3)_2{\cdot}4H_2O$.

All catalyst precursors, MnO_x-promoted and not promoted, prepared by IMP and SEA methods were thermally treated and reduced. First, these materials were thermally treated under a He flow (60 mL min^{-1}) from room temperature to 350 ºC with a heating rate of 5 ºC min^{-1}, and maintained at that temperature for 1 h. Next, the carrier gas was shifted to H_2 (60 mL min^{-1}), cooled down to 300 ºC, and that temperature was kept for 3 h in order to reduce mainly the copper species. Then, the gas was changed to He again, and the sample was maintained at 300 ºC for 1 h before cooling it down to room temperature under He flow. Finally, the reduced species were passivated using 0.5% O_2/N_2 for 30 min at room temperature. Those series of catalysts were denoted as $1Cu_{IMP}$:zMn_{IMP} and $1Cu_{SEA}$:zMn_{IMP}, respectively.

Finally, another family of materials was synthesized by adding Cu by SEA and MnO_x species by CSR methods. First, a 15 wt% Cu/SiO_2 catalyst precursor was prepared by the SEA method described before. Then, the sample was reduced in a Schlenk tube by increasing the temperature from room temperature to 300 ºC under He, followed by a change in the carrier gas to H_2 while keeping the temperature constant (300 ºC) for 3 h. After that, the sample was cooled down to room temperature under H_2 flow, and without passivation, the Schlenk tube was sealed and transferred to a glove box filled with Ar. Later, the sample was put in contact with a solution containing the amount of cyclopentadienyl manganese(I) tricarbonyl ($C_5H_5Mn(CO)_3$) necessary for a Cu:Mn atomic ratio = 1:0.15 in anhydrous tetrahydrofuran for 1 h under stirring, as described elsewhere [38]. Hence, MnO_x species should be selectively adsorbed onto the reduced Cu nanoparticles. After that, the solvent was removed in a Schlenk line and the sample was reduced again at 400 ºC (1 ºC min^{-1} ramp) for 1 h under H_2 flow to ensure the decomposition of the ligands, being subsequently cooled down to room temperature under

reducing atmosphere (1 CSR cycle). In the case of the $1Cu_{SEA}$:$0.15Mn_{CSR}$ catalyst, metal species were then passivated under 0.5% O_2/N_2) for 30 min at room temperature. However, for the synthesis of the$1Cu_{SEA}$:$0.30Mn_{CSR}$ and $1Cu_{SEA}$:$0.45Mn_{CSR}$ catalysts, MnO_x loadings were increased by the sequential addition of CSR cycles (2 and 3 CSR cycles) without intermediate passivation. After the last CSR cycle, samples were passivated as shown for the $1Cu_{SEA}$:$0.15Mn_{CSR}$ catalyst.

2.3. Catalyst Characterization

Powder X-ray diffraction patterns were obtained using an X-Pert Pro automated diffractometer, which is composed of a Ge (111) primary monochromator with Cu Kα1 radiation and a X'Celerator detector with a step size of 0.017º. The analysis was carried out between 2θ = 10-70º, with an equivalent counting time of 712 s per step. The crystallite size was calculated by using the Williamson-Hall equation [40], $B\cos\theta = (K\lambda/D) + (2\varepsilon\sin\theta)$, where θ is the Bragg angle, B is the full width at half maximum (FWHM) of the XRD peaks, K is the Scherrer constant, λ is the wavelength of the X-ray, and ε is the lattice strain.

H_2 temperature-programmed reduction (H_2-TPR) experiments were performed using 80 mg of catalyst in a U-shaped reactor. First, catalyst precursors were treated under a He flow (60 mL min^{-1}) up to 350 ºC (5 ºC min^{-1} ramp) for 1 h to decompose the precursor salt and avoid the contamination of the equipment. After this, the catalyst was cooled down to room temperature to start the analysis. The sample was then heated from room temperature to 800 ºC with (10 ºC min^{-1} ramp) under H_2/Ar (48 mL min^{-1}, 10 vol.% H_2) to study the H_2 consumption. In addition, the outcoming flow was passed through a cold finger immersed in an isopropyl alcohol−liquid nitrogen trap to retain the water formed during the reduction process. Finally, an on-line thermal conductivity detector (TCD) was used to perform the H_2 quantification.

Transmission electron microscopy (TEM) images were obtained by using a FEI Talos F200x high-resolution transmission electron microscope (Thermo Fisher Scientific) to study the morphology and dispersion of the active phase. Moreover, elemental microanalysis was carried out with an EDX Super-X system with four X-ray detectors and a X-FEG beam, which allows for 3D chemical characterization with compositional mapping.

Textural parameters were obtained from N_2 adsorption–desorption at -196 ºC by using an automated ASAP 2420 Micromeritics equipment. Firstly, samples were outgassed at 150 ºC for 12 h at 10^{-4} mbar. The Brunauer–Emmet–Teller (BET) method was utilized to determine the specific surface areas [41], the specific pore volume (Vs) was calculated at $P/P_0 = 0.98$, the pore size distribution was obtained using a DFT method [42], and finally, the average pore size was determined by applying the Barrett–Joyner–Halenda (BJH) method to the desorption branch [43].

In order to study the surface composition of the catalysts, all of them were analyzed by X-ray photoelectron spectroscopy (XPS). The analyses were performed in a Physical Electronics PHI 5700 spectrometer with non-monochromatic Mg Kα radiation (300 W, 15 kV, 1253.6 eV) with a multichannel detector. Spectra were recorded using the constant pass energy mode at 29.35 eV with a 720 μm diameter analysis area. The maximum peak of adventitious carbon was used as the reference for the different peaks (C 1s at binding energy of 284.8 eV). Moreover, a PHI ACCESS ESCA-V6.0 F software package was used for acquisition and data analysis. The peaks were deconvoluted by using the least squares method, Gaussian–Lorentzian (90% G and 10% L) curves to more accurately determine the binding energy (BE) values of the different element core levels, and a Shirley-type background line. To avoid the oxidation of the reduced catalysts, these were stored in sealed vials with cyclohexane as inert solvent. Moreover, samples were handled in a dry box under a N_2 flow, where the solvent was evaporated prior to its introduction into the analysis chamber, and directly analyzed without previous treatment.

2.4. Catalytic test

The gas-phase hydrogenation of furfural was carried out at atmospheric pressure in a tubular quartz reactor with a diameter of 6.35 mm (¼"). For each experiment, the catalyst was pelletized and sieved with a range between 215 and 400 μm. Each sample was placed in the middle of the reactor tube between two layers of quartz wool, and the temperature was controlled with a thermocouple in direct contact with the catalyst bed. Prior to the catalytic tests, the passivated catalysts were reduced *in situ* at 300 ºC using a H_2 flow of 60 mL min^{-1} for 1 h to ensure the total reduction of Cu(II) species. Then, catalysts were cooled down to the selected reaction temperature. Once at that temperature, 3.87 mL h^{-1} of a FUR solution in CPME (5 vol.%) was injected continuously with a Gilson 307SC piston pump (model 10SC) to obtain a weight hourly space velocity (WHSV) of 1.5 h^{-1} (referred to the FUR fed) using 10–60 mL min^{-1} of H_2 as the carrier

gas. CPME was selected as the solvent because it is considered environmentally friendly and has employed in several reactions for biomass valorization, such as the selective dehydration of lignocellulosic pentoses to FUR [44]. The CPME stability was evaluated under experimental conditions similar to those used in the gas-phase furfural hydrogenation, thus confirming the inertness of CPME regardless of the catalyst used.

Both furfural and reaction products were analyzed using a Shimadzu GC-14A gas chromatograph equipped with a flame ionization detector and a CP-Wax 52CB capillary column. The furfural conversion and product selectivity were calculated as follows:

$$\text{Conversion (\%)} = \frac{\text{mol of furfural converted}}{\text{mol of furfural fed}} \times 100$$

$$\text{Selectivity (\%)} = \frac{\text{mol of product}}{\text{mol of furfural converted}} \times 100$$

3. Results and Discussion

3.1. Characterization of the catalysts

In order to determine the reduction temperature, H_2-TPR analyses of the catalyst precursors were carried out (Figure 1). From these profiles, it can be inferred that CuO was totally reduced to Cu^0 at 325 ºC. The maximum H_2 consumption occurred at about 235 ºC, which is in the same range as other catalysts with small CuO nanoparticles supported on silica in the literature [45]. It is noteworthy that the addition (by impregnation) of Mn species to Cu/SiO_2 samples prepared by impregnation (IMP) or strong electrostatic adsorption (SEA) produces an increase in the H_2 consumption, as can be observed from the higher area of the H_2-TPR profiles. This implies that, besides reducing Cu species, MnO_x formed during the thermal treatment of $Mn(NO_3)_2{\cdot}4H_2O$ must have also been partially reduced, although their reduction profiles barely changed. However, the maximum H_2 consumption for the $1Cu_{SEA}$:$0.15Mn_{IMP}$ and $1Cu_{IMP}$:$0.15Mn_{IMP}$ samples shifted to lower temperatures, probably due to the presence of oxygen vacancies from MnO_x species that would enhance the reducibility of CuO, as previously reported by other authors [46]. As a result, as previously mentioned, all those catalyst precursors were reduced at 300 ºC for 1 h to ensure the total reduction of the Cu species. It is worth mentioning that the $1Cu_{SEA}$:$0.15Mn_{CSR}$ precursor was not characterized by H_2-TPR because the reduction process would also be accompanied by the decomposition of the organometallic precursor ligands. Since it was reported in the

literature that the decomposition of a similar organomanganese compound (methylcyclopentadienyl manganese tricarbonyl) bonded to silica occurred at temperatures above 300 ºC[47], a reduction temperature of 400 ºC was selected for that catalyst to ensure both the ligands decomposition and reduction of the Cu species.

Commented [ACAR1]: Por favor cita este articulo: https://pubs.acs.org/doi/10.1021/om5006269.

Structural information of the Cu- and Cu-MnO_x-based catalysts was obtained by XRD (Figure 2). In all cases, the diffractograms presented a broad band at about 2θ = 22º, which is associated with the amorphous silica support [45]. Furthermore, all XRD patterns showed two main narrow peaks at 43.2 and 50.4º, which are assigned to metal Cu crystallites (Cu^0) (PDF 96-901-2044). In addition, a small and broad diffraction band at 35.9º could be due to the presence of Cu_2O (PDF:01-078-2076). The coexistence of Cu^0 and Cu_2O species could be due to Cu(II) species that were not totally reduced. On the other hand, it is also noticeable that the diffractograms did not show diffraction peaks evidencing the existence of crystalline Mn species; therefore, these are amorphous or highly dispersed. Moreover, it was observed that metal copper nanoparticles are more crystalline, thus have a larger average crystallite sizes, when Cu and Mn precursors are incorporated to the support by impregnation ($1Cu_{IMP}$:$0.15Mn_{IMP}$).

The average size of the Cu^0 crystallites was determined by the Williamson-Hall method [40], being this of 24 nm for the Cu_{SEA} catalyst. A similar value was obtained for the $1Cu_{IMP}$:$0.15Mn_{IMP}$ catalyst. However, when Cu was incorporated by the SEA method followed by the addition of MnO_x by impregnation ($1Cu_{SEA}$:$0.15Mn_{IMP}$) or CSR method ($1Cu_{SEA}$:$0.15Mn_{CSR}$), the average size of the Cu^0 crystallites diminished to 16 and 18 nm, respectively. Therefore, it can be inferred that the incorporation of Mn species, either by impregnation or CSR, diminishes the size of the Cu^0 crystallites obtained by the SEA method. Regarding the analysis of the Cu_2O domains, all catalysts displayed similar average size around 5-8 nm. According to the H_2-TPR curves (Figure 1), the maximum H_2 consumption occurred at 225-250 ºC; therefore, it is possible that the selected reduction temperature (400 ºC) could have contributed to sintering of the Cu nanoparticles.

The morphology of the Cu-MnO_x-based catalysts was studied by TEM (Figure 3). These micrographs revealed that the Cu_{SEA} catalyst displayed a heterogeneous dispersion of Cu nanoparticles, with sizes extending from <10 to 30 nm, which is consistent with the broad H_2 consumption observed in the corresponding H_2-TPR curve. The wider H_2-TPR profile compared to those of the Cu-MnO_x-based catalysts suggests a broader

distribution of Cu particle sizes. When MnO_x species are dispersed onto the catalysts , it is expected that CuO and MnO_x domains are in intimate contact before the reduction process, thus MnO_x could contribute to decreasing the reduction temperature of the Cu(II) species due to the presence of oxygen vacancies [48,49].

The textural properties of the Cu-MnO_x-based catalysts were determined from their N_2 adsorption-desorption isotherms at -196 ºC (Figure 4). The adsorption isotherms were very similar in all cases regardless of the approach used for the incorporation of Cu species and the presence of MnO_x, which implies that the synthesis method does not have a significant effect in their textural properties. According to the IUPAC classification [50], the adsorption-desorption isotherms can be considered as Type II, which are typical of macroporous materials with an increased volume of N_2 adsorbed at high relative pressure. This fact must be ascribed to the spherical nature of the fumed silica used as the support, which contains macropores associated to interparticle voids.

The specific surface areas (S_{BET}) were determined using the BET method (Table 1) [41], and showed to be very similar (155-188 m^2/g), with low microporosity as indicated by the t-plot values. The pore volume (Table 1) was also very close for all catalysts, ranging between 0.524 and 0.540 cm^3/g with negligible microposity. From these data, it can be concluded that all catalysts displayed similar textural characteristics despite the synthesis method.

The surface chemical composition and oxidation state of the Cu and Mn species on the Cu-MnO_x-based catalysts was evaluated by XPS (Table 2 and Figure 5). The surface Cu atomic content is in the 0.65-1.88% range, being $1Cu_{IMP}$:$0.15Mn_{IMP}$ the catalyst with the lowest surface Cu content. This implies that the conventional incipient wetness impregnation method provides lower metal dispersion, thus larger Cu nanoparticles, as was determined from the Williamson-Hall method [40]. In contrast, the highest surface Cu content was obtained with the SEA method, which highlights the potential of this approach for the highly dispersion of Cu nanoparticles on the silica surface. On the other hand, the incorporation of MnO_x species causes a decrease in the surface Cu content, likely due to the partial coverage of the Cu nanoparticles, as observed by TEM (Figure 3). Interestingly, the $1Cu_{SEA}$:$0.15Mn_{CSR}$ catalyst presented the lowest surface Mn concentration (Table 2), which would indicate that MnO_x was not selectively deposited onto the Cu nanoparticles, if not also dispersed over the silica support. Sener et

al. attributed that to the reaction between the organometallic precursor and the hydroxyl groups on the silica support [51].

Commented [ACAR2]: Por favor cita este articulo: https://pubs.acs.org/doi/abs/10.1021/acscatal.5b02028.

The analysis of the Cu 2p core level spectra shows a similar pattern for all catalysts (Figure 5A). All Cu-MnO_x-based catalysts display a single band in the Cu $2p_{3/2}$ region, which is located at about 932.5 eV. This signal is ascribed to the presence of reduced Cu species [52]. On the other hand, the absence of the characteristic shake-up satellite would discard the existence of surface Cu^{2+} species. Although it is difficult to discern between the reduced Cu^0 and Cu^+ species from the Cu 2p region, it is possible to draw on the Auger LMM line (Figure 5B). The analysis of this region shows the coexistence of Cu^0 and Cu^+, being mostly Cu^+ in the form of Cu_2O (about 60-70% Cu). These results seem to contradict those obtained by XRD (Figure 2), where the main crystalline phase was Cu^0. Considering the H_2-TPR profiles (Figure 1), it should be expected that all Cu species are totally reduced, so the detection of Cu^+ species in the XRD patterns (Figure 2) and the Cu_{LMM} Auger line (Figure 5B) should be ascribed to a partial oxidation during handling of the sample. Nonetheless, the data obtained from XRD and XPS differ, since the main crystalline phase seems to be Cu^0 but the XPS data suggest the primary presence of Cu_2O. This can be attributed to the fact that XPS is a surface technique and the oxidation of Cu^0 is expected to take place mainly on the catalyst surface.

The analysis of the Mn 2p core level spectra also shows a similar profile for all catalysts (Figure 5C). Although the band at the lowest binding energy (~641.8 eV) has been previously assigned to the presence of Mn_xO_y species [52], the typical contributions of MnO, Mn_2O_3, and MnO_2 in the Mn 2p core level spectra appear very close [52]. Nonetheless, it can be observed another contribution located at about 646.6 eV, which is assigned to the shake-up satellite that is typical of divalent cations, such as Mn^{2+} [53]. Thus, it is confirmed the existence of Mn(II) species, although the presence of higher oxidation states, such as Mn_3O_4 or Mn_2O_3, cannot be ruled out. These data could prove the simultaneous reduction of CuO and partial reduction of MnO_2 species, as was suggested from the H_2-TPR experiments (Figure 1).

From the Si 2p core level spectra, it can be observed a contribution at about 103.2-103.4 eV, which is assigned to silica [45]. Finally, the O 1s spectra show two contributions: the higher one at 532.6 eV is ascribed to oxygen in silica [45], while that at lower binding energy (530.2 eV) is attributed to oxygen in the MnO_x species [52,54].

3.2. Catalytic Results

All Cu- and Cu-MnO_x-based catalysts were studied in the hydrogenation of FUR in a continuous gas-phase reactor. As mentioned before, the stability of CPME was confirmed in previous studies under similar experimental conditions. The catalytic results (Figure 6A) show that the highest conversion was obtained with the Cu_{SEA} catalyst, with almost full FUR conversion after 1 h at 190 ºC, although this slightly dropped with time, attaining a 95% conversion after 5 h. Although, in general, the incorporation of MnO_x species worsened the FUR conversion, the reduction of the activity depended on the methodology used for the incorporation of those MnO_x species. For example, the incorporation of MnO_x by impregnation ($1Cu_{SEA}$:$0.15Mn_{IMP}$) only led to a slight decrease in the FUR conversion (85% after 5 h) in comparison to the monometallic Cu_{SEA} catalyst. However, the drop in the conversion was more pronounced when MnO_x was incorporated by the CSR method ($1Cu_{SEA}$:$0.15Mn_{CSR}$), since this only reached a FUR conversion of 40% after 5 h of reaction. Even when that catalyst displayed the highest proportion of surface Cu species, it seems like the lack of interaction between Cu and MnO_x species contributed to the poorest conversion values. These data suggest that the interaction between the MnO_x species and Cu^0 must cause an electronic transfer, as suggested the H_2-TPR, with an important effect on the catalytic behavior. Additionally, it was observed that the the incorporation of Cu by the SEA method ($1Cu_{SEA}$:$0.15Mn_{IMP}$) contributed to higher FUR conversion values than impregnation ($1Cu_{IMP}$:$0.15Mn_{IMP}$). As the Cu dispersion is higher when using the SEA method than the impregnation, it is believed that upon addition of MnO_x species, there is a higher proportion of metal Cu sites interacting with MnO_x species, as well as a higher concentration of sites involved in FUR hydrogenation.

Regarding the selectivity patterns (Figures 6B and 6C), all catalysts showed to be selective only towards two products: furfuryl alcohol (FOL) and 2-methylfuran (MF). As the FOL and MF yields vary for the different catalysts, it is suggested that the presence and dispersion of the MnO_x species must have an important role in determining the selectivity profiles. In the case of Cu_{SEA}, the main product is MF, although its yield decreases along the time-on-stream (TOS) at 190 ºC from 88% after 1 h of reaction to 71% after 5 h. This drop in the MF yield was accompanied by an increase in the FOL yield, and it is consistent with prior studies in which highly dispersed Cu/SiO_2 catalysts promoted the formation of MF especially at short reaction times [32,45]. It was previously

reported that the hydrogenation of FUR to FOL required the existence of Cu^0 or Cu^+ sites [27,55,56], although there is still controversy in the literature regarding the active sites involved in FUR hydrogenation. Some studies have proposed that Cu^0 sites interact with the carbonyl group leading to the hydrogenation of FUR to FOL [27,55]. However, other authors have pointed out that the electrophilic Cu^+ species can also promote the hydrogenation reaction because –C=O can be polarized due to the lone pair electrons on the O atom interacting with Cu^+ sites [57,58]. The presence of oxygen vacancies on the surface of the catalyst can also provide a higher hydrogenating capacity due to Mn^{2+}-O_v-Mn^{2+} defect structures that can interact with the carbonyl group of FUR, weakening the –C=O bond and promoting the FUR hydrogenation [37,59].

In addition, the nature of the support can also play an important role on both the catalytic activity and selectivity [60]. Thus, the presence of a support with low acidity, such as SiO_2, and small Cu nanoparticles, which can be partially oxidized to Cu^+, provides Lewis acid sites that promote the hydrogenolysis of FOL to MF [27]. Interestingly, the incorporation of MnO_x species appears to modify the selectivity pattern, since they seem to favor the formation of FOL to the detriment of MF. Previous studies have reported that the presence of reducible oxides, such as CeO_2 or MnO_2, can generate oxygen vacancies, leading to a decay of structural oxygen from the anion sublattice [37,61] and promoting its interaction with the carbonyl group of FUR to produce FOL as the main product [18,37,62]. Therefore, the modification of the selectivity pattern can be ascribed to the presence of well-dispersed Cu nanoparticles and the reduction of Mn^{4+} to $Mn^{2/3+}$, which generates surface oxygen vacancies, $Mn^{2/3+}$-O_v-$Mn^{2/3+}$, associated to structural defects [37]. On the other hand, the modification of the electronic density of the Cu sites, as suggested from the H_2-TPR profiles (Figure 1), together with its lower surface Cu content, could contribute to a reduction of the hydrogenolysis process, thus decreasing the MF formation. Thereby, it can be concluded that the incorporation of Mn species in the form of MnO_x (with oxidation states lower than +4) would promote the hydrogenation reaction to FOL.

On the other hand, it is well known that the hydrogenation of FUR is prone to suffer from deactivation processes [16]. For example, carbonaceous deposits tend to block the active sites involved in the hydrogenolysis reaction faster than the hydrogenation sites, thus promoting the formation of FOL [45]. As $1Cu_{SEA}$:$0.15Mn_{IMP}$ showed the highest FOL yield after 5 h of TOS at 190 ºC, that synthesis approach,

involving the incorporation of Cu by SEA and Mn by IMP method, was selected to study the effect of the Mn:Cu atomic ratio between 0.15 and 0.45 (Figure 7).

The catalytic results show that the presence of a higher proportion of Mn species leads to a lower catalytic activity, since the FUR conversion after 5 h at 190 ºC is 95% with Cu_{SEA} and 53% when using the catalyst with the highest Mn content ($1Cu_{SEA}$:$0.45Mn_{IMP}$ catalyst). The yields towards FOL and MF also differ with the MnO_x loading, since higher Mn contents seem to favor the formation of FOL, with $1Cu_{SEA}$:$0.45Mn_{IMP}$ and $1Cu_{SEA}$:$0.30Mn_{IMP}$ showing FOL yields close to 50% after 1 h at 190 ºC. Remarkably, those catalysts maintained those FOL yields for at least 5 h of reaction at 190 ºC, although some deactivation was observed. Similarly, the study of the MF yield shows a decrease as the Mn content increases, thus confirming that MnO_x has an influence in the selectivity pattern. In this sense, the oxygen vacancies generated on the surface of the catalyst promotes the hydrogenation due to the interaction of these vacancies with the carbonyl group of FUR [37]. Similar results were reported in the literature when using CeO_2 as the support, which also favored the formation of oxygen vacancies that modified the selectivity from MF to FOL [18,33,34].

After evaluating the catalytic activity of Cu_{SEA}:Mn_{IMP} with different Mn:Cu atomic ratios, the materials were characterized to establish structure-activity relationships. The analysis of their H_2-TPR profiles (Figure 8) shows how the maximum H_2 consumption takes place at temperatures slightly lower than that for Cu_{SEA}. These data would confirm that the formation of oxygen vacancies during the reduction of MnO_2 to MnO_x could provoke a modification in the reducibility of the CuO particles, which could be due to the intimate contact between CuO and MnO_2 phases before reduction [46]. It is also remarkable that the H_2 consumption varies with the Cu:Mn atomic ratio. As the $1Cu_{SEA}$:$0.15Mn_{IMP}$ catalysts exhibits a higher H_2 consumption than Cu_{SEA}, it is expected that, besides the reduction of CuO, MnO_2 must also be partially reduced. This fact is more pronounced for $1Cu_{SEA}$:$0.30Mn_{IMP}$, where the H_2 consumption is higher although the surface Cu content is similar (Table 3). In the case of the catalyst with the highest Mn content ($1Cu_{SEA}$:$0.45Mn_{IMP}$), several H_2 consumption processes at are observed at lower temperatures, while the maximum H_2 consumption is higher than that for Cu_{SEA}, which would confirm the simultaneous reduction of CuO and MnO_2.

The XRD analysis of the catalysts with different Mn:Cu atomic ratios (Figure 9) revealed similar profiles. The main peaks located at 43.4 and 50.6º are assigned to Cu^0

(PDF 96-901-2044), while the small and broad band at 35.6º is attributed to Cu_2O crystallites (PDF:01-078-2076). The estimation of the crystal size from the Williamson-Hall method reveals that the size of the crystal diminishes as the Mn-content increases [40]. Thus, the average Cu^0 crystallite size progressively decreases from 24 nm for Cu_{SEA} to 13 nm for $1Cu_{SEA}$:$0.45Mn_{IMP}$. Regarding the average crystal size of Cu_2O, all catalysts showed an average crystallite size below 8 nm. As before, the diffractograms do not exhibit any diffraction peaks assigned to Mn species, which can be attributed to poor crystallinity or even amorphous particles.

TEM micrographs also reveal that both Cu and Mn species are highly dispersed (Figure 10) even for high Mn contents. Therefore, Cu^0 nanoparticles and MnO_x species must be in close contact, as inferred from the H_2-TPR data, with the oxygen vacancies of MnO_x contributing to the reduction of the CuO species at lower temperatures (Figure 8). On the other hand, the study of the textural properties again evidenced that all catalysts possessed similar characteristics (Table 4), which means that the incorporation of Cu and MnO_x species did not significantly modify the textural properties of the silica support.

The surface chemical composition of the Cu_{SEA}:Mn_{IMP} catalysts with different Mn:Cu atomic ratios was determined by XPS (Figure 11 and Table 3). All the catalysts exhibit reduced Cu species, although the Cu_{LMM} Auger lines show the coexistence of both Cu^0 and Cu^+. Regarding to the Mn 2p core level spectra, the catalysts with different Mn:Cu atomic ratios showed similar contributions. The main band is assigned to the existence of Mn(II), likely MnO, as confirmed by the shake-up satellite typical of divalent cations, although the presence of other contributions, such as Mn_2O_3 or Mn_3O_4, cannot be discarded since the binding energies of Mn(II) and Mn(III) are very close.

In a final study, all Cu-MnO_x-based catalysts with a Mn:Cu atomic ratio of 0.15 were tested for long reaction times to evaluate their stability (Figure 12). Although all catalysts showed a FUR conversion decay after the first hours of the reaction, the deactivation was more pronounced on the catalysts with the highest surface Mn contents ($1Cu_{IMP}$:$0.15Mn_{IMP}$ and $1Cu_{SEA}$:$0.15Mn_{IMP}$) (Table 2). However, after 24 h of TOS, those catalysts still provided higher FUR conversions than $1Cu_{SEA}$:$0.15Mn_{CSR}$, which was the catalyst containing the lowest surface Mn content (Table 2). The selectivity pattern is also modified along the reaction. Thus, the catalysts with high dispersion of Cu species, i.e., those prepared by the SEA method, favors the formation of MF. However, the catalysts with the lowest surface Mn content ($1Cu_{SEA}$:$0.15Mn_{CSR}$) not only presented the lowest

FUR conversion, but also the MF yield. In any case, the formation of MF decreases drastically along the TOS, being negligible after 24 h of reaction, which further highlights the faster deactivation of the hydrogenolysis sites. After the incorporation of MnO_x species, the MF formation decreases, which would be associated to the oxygen vacancies on MnO_x that would promote the hydrogenation of FUR to FOL. Interestingly, in all cases except for the $1Cu_{SEA}$:$0.15Mn_{CSR}$ catalyst, the FOL yield increased after the first hours of reaction. From these data, it can be inferred that the hydrogenolysis sites are more easily deactivated than those responsible for the hydrogenation of FUR to FOL. Nonetheless, the FOL yield also drops from about 60% after 8 h of TOS to 35% after 24 h for $1Cu_{SEA}$:$0.15Mn_{IMP}$, which showed to be the most resistant catalyst to deactivation.

4. Conclusions

Cu-MnO_x-based catalysts supported on commercial silica were synthesized using different methods, such as incipient wetness impregnation, strong electrostatic adsorption, and controlled surface reactions. Catalyst characterization revealed that the strong electrostatic adsorption method provided the highest dispersion of Cu nanoparticles while the impregnation of Mn species generated the closest interaction between Cu and MnO_x. H_2-TPR studies showed that the presence of MnO_2 in the catalytic precursor facilitated the reducibility of the Cu species at lower temperatures. Likewise, it was observed that the H_2 consumption increased, which can be attributed to the partial reduction of MnO_2 to MnO_x, as was confirmed by XPS.

In regards to the catalytic activity, the presence of MnO_x species promoted the hydrogenation of FUR to FOL, rather than the hydrogenolysis reaction to form MF. In this sense, the hydrogenation reaction is promoted by the presence of Mn^{2+}-O_v-Mn^{2+} defects, which favors the interaction of the oxygen vacancies with the carbonyl group, weakening the –C=O bond, and promoting the FUR hydrogenation. In any case, all catalysts were prone to deactivation due to the formation of carbonaceous deposits that partially blocked the active sites for reaction.

Author Contributions

Conceptualization, J.A.C., A.C.A-R.; methodology, J.A.C., A.C.A-R., A.C., C.G-S., P.M-T.; software, J.A.C., C.P.J-G.; validation, J.A.C., C.G-S., R.M-T.; formal analysis,

J.A.C, C.G-S.; investigation, C.P.J-G.; resources, A.C.A-R., P.M-T.; data curation, J.A.C.; writing-original draft preparation, J.A.C., C.P.J-G.; writing-review and editing, J.A.C., A.C.A-R., R.M-T., P.M-T.; visualization, A.C.A-R., R.M-T., P.M-T.; supervision, A.C.A-R., R.M-T., P.M-T.; project administration, A.C.A-R., R.M-T., P.M-T.; funding acquisition, A.C.A-R., R.M-T., P.M-T.

Funding

The authors acknowledge financial support from the Spanish Ministry of Science, Innovation and Universities (PID2021-122736OB-C42 project), FEDER (European Union) funds (UMA18-FEDERJA-171 and UMA20-FEDERJA-88), Junta de Andalucía (P20-00375), and the University of Malaga. C.P.J-G. and C.G-S. acknowledge Junta de Andalucía and FEDER funds, respectively, for their postdoctoral contracts. A.C.A-R. is thankful to the University of Toledo for her start-up package. Funding for open access article processing charge was provided by the University of Malaga/CBUA.

Institutional Review Board Statement

Not applicable

Informed Consent Statement

Not applicable.

Data Availability Statement

The authors confirm that all data generated or analyzed during this study are available from the corresponding author. These materials can be requested directly from the corresponding author if needed.

Conflicts of Interest

The authors declare no conflict of interest. The funders had no role in the design of the study; in the collection, analyses, or interpretation of data; in the writing of the manuscript, or in the decision to publish the results.

References

[1] J.P. Lange, E. Van Der Heide, J. Van Buijtenen, R. Price, Furfural-A promising platform for lignocellulosic biofuels, ChemSusChem. 5 (2012) 150–166. https://doi.org/10.1002/cssc.201100648.

[2] R. Mariscal, P. Maireles-Torres, M. Ojeda, I. Sádaba, M. López Granados, Furfural: A renewable and versatile platform molecule for the synthesis of chemicals and fuels, Energy Environ. Sci. 9 (2016) 1144–1189. https://doi.org/10.1039/c5ee02666k.

[3] E. Parlament, Directive of the European Parlament and of the Council on the Promotion of the Use of Energy for Renewable Sources, (2008).

[4] R. Dittmeyer, M. Klumpp, P. Kant, G. Ozin, Crowd oil not crude oil, Nat. Commun. 10 (2019) 1818. https://doi.org/10.1038/s41467-019-09685-x.

[5] M.F. Kuehnel, E. Reisner, Solar Hydrogen Generation from Lignocellulose, Angew. Chemie - Int. Ed. 57 (2018) 3290–3296. https://doi.org/10.1002/anie.201710133.

[6] S.D. Shinde, X. Meng, R. Kumar, A.J. Ragauskas, Recent advances in understanding the pseudo-lignin formation in a lignocellulosic biorefinery, Green Chem. 20 (2018) 2192–2205. https://doi.org/10.1039/c8gc00353j.

[7] T. Wang, M.W. Nolte, B.H. Shanks, Catalytic dehydration of C6 carbohydrates for the production of hydroxymethylfurfural (HMF) as a versatile platform chemical, Green Chem. 16 (2014) 548–572. https://doi.org/10.1039/c3gc41365a.

[8] C. García-Sancho, I. Agirrezabal-Telleria, M.B. Güemez, P. Maireles-Torres, Dehydration of d-xylose to furfural using different supported niobia catalysts, Appl. Catal. B Environ. 152–153 (2014) 1–10. https://doi.org/10.1016/j.apcatb.2014.01.013.

[9] L. Hu, G. Zhao, W. Hao, X. Tang, Y. Sun, L. Lin, S. Liu, Catalytic conversion of biomass-derived carbohydrates into fuels and chemicals via furanic aldehydes, RSC Adv. 2 (2012) 11184–11206. https://doi.org/10.1039/c2ra21811a.

[10] K.J. Zeitsch, The chemistry and technology of furfural and its many by-products, Elsevier, Amsterdam. The Netherlands, 2000.

[11] K. Yan, G. Wu, T. Lafleur, C. Jarvis, Production, properties and catalytic hydrogenation of furfural to fuel additives and value-added chemicals, Renew. Sustain. Energy Rev. 38 (2014) 663–676. https://doi.org/10.1016/j.rser.2014.07.003.

[12] X. Li, P. Jia, T. Wang, Furfural: A Promising Platform Compound for Sustainable Production of C4 and C5 Chemicals, ACS Catal. 6 (2016) 7621–7640. https://doi.org/10.1021/acscatal.6b01838.

[13] C. Wang, H. Xu, R. Daniel, A. Ghafourian, J.M. Herreros, S. Shuai, X. Ma, Combustion characteristics and emissions of 2-methylfuran compared to 2,5-dimethylfuran, gasoline and ethanol in a DISI engine, Fuel. 103 (2013) 200–211. https://doi.org/10.1016/j.fuel.2012.05.043.

[14] X. Ma, C. Jiang, H. Xu, H. Ding, S. Shuai, Laminar burning characteristics of 2-methylfuran and isooctane blend fuels, Fuel. 116 (2014) 281–291. https://doi.org/10.1016/j.fuel.2013.08.018.

[15] M. Thewes, M. Muether, S. Pischinger, M. Budde, A. Brunn, A. Sehr, P. Adomeit, J. Klankermayer, Analysis of the impact of 2-methylfuran on mixture formation and combustion in a direct-injection spark-ignition engine, Energy and Fuels. 25 (2011) 5549–5561. https://doi.org/10.1021/ef201021a.

[16] D. Liu, D. Zemlyanov, T. Wu, R.J. Lobo-Lapidus, J.A. Dumesic, J.T. Miller, C.L. Marshall, Deactivation mechanistic studies of copper chromite catalyst for

selective hydrogenation of 2-furfuraldehyde, J. Catal. 299 (2013) 336–345. https://doi.org/10.1016/j.jcat.2012.10.026.
[17] H. Adkins, R. Connor, The catalytic hydrogenation of organic compounds over copper chromite, J. Am. Chem. Soc. 53 (1931) 1091–1095. https://doi.org/10.1021/ja01354a041.
[18] C.P. Jiménez-Gómez, J.A. Cecilia, I. Márquez-Rodríguez, R. Moreno-Tost, J. Santamaría-González, J. Mérida-Robles, P. Maireles-Torres, Gas-phase hydrogenation of furfural over Cu/CeO2 catalysts, Catal. Today. 279 (2017) 327–338. https://doi.org/10.1016/j.cattod.2016.02.014.
[19] S. Sitthisa, D.E. Resasco, Hydrodeoxygenation of furfural over supported metal catalysts: A comparative study of Cu, Pd and Ni, Catal. Letters. 141 (2011) 784–791. https://doi.org/10.1007/s10562-011-0581-7.
[20] C.P. Jiménez-Gómez, J.A. Cecilia, R. Moreno-Tost, P. Maireles-Torres, Nickel Phosphide/Silica Catalysts for the Gas-Phase Hydrogenation of Furfural to High-Added-Value Chemicals, ChemCatChem. 9 (2017) 2881–2889. https://doi.org/10.1002/cctc.201700312.
[21] M. Hronec, K. Fulajtarová, T. Liptaj, Effect of catalyst and solvent on the furan ring rearrangement to cyclopentanone, Appl. Catal. A Gen. 437–438 (2012) 104–111. https://doi.org/10.1016/j.apcata.2012.06.018.
[22] K. An, N. Musselwhite, G. Kennedy, V. V. Pushkarev, L. Robert Baker, G.A. Somorjai, Preparation of mesoporous oxides and their support effects on Pt nanoparticle catalysts in catalytic hydrogenation of furfural, J. Colloid Interface Sci. 392 (2013) 122–128. https://doi.org/10.1016/j.jcis.2012.10.029.
[23] E. Ricard, H.M. Guinot, US patent 17309919, (1929).
[24] R.S. Rao, R.T.K. Baker, M.A. Vannice, Furfural hydrogenation over carbon-supported copper, Catal. Letters. 60 (1999) 51–57.
[25] D. Vargas-Hernández, J.M. Rubio-Caballero, J. Santamaría-González, R. Moreno-Tost, J.M. Mérida-Robles, M.A. Pérez-Cruz, A. Jiménez-López, R. Hernández-Huesca, P. Maireles-Torres, Furfuryl alcohol from furfural hydrogenation over copper supported on SBA-15 silica catalysts, J. Mol. Catal. A Chem. 383–384 (2014) 106–113. https://doi.org/10.1016/j.molcata.2013.11.034.
[26] B.M. Nagaraja, V. Siva Kumar, V. Shasikala, A.H. Padmasri, B. Sreedhar, B. David Raju, K.S. Rama Rao, A highly efficient Cu/MgO catalyst for vapour phase hydrogenation of furfural to furfuryl alcohol, Catal. Commun. 4 (2003) 287–293. https://doi.org/10.1016/S1566-7367(03)00060-8.
[27] Y. Shi, Y. Zhu, Y. Yang, Y.W. Li, H. Jiao, Exploring Furfural Catalytic Conversion on Cu(111) from Computation, ACS Catal. 5 (2015) 4020–4032. https://doi.org/10.1021/acscatal.5b00303.
[28] H. Du, X. Ma, P. Yan, M. Jiang, Z. Zhao, Z.C. Zhang, Catalytic furfural hydrogenation to furfuryl alcohol over Cu/SiO2 catalysts: A comparative study of the preparation methods, Fuel Process. Technol. 193 (2019) 221–231. https://doi.org/10.1016/j.fuproc.2019.05.003.
[29] C.P. Jiménez-Gómez, J.A. Cecilia, A.C. Alba-Rubio, A. Cassidy, R. Moreno-Tost, C. García-Sancho, P. Maireles-Torres, Tailoring the selectivity of Cu-based catalysts in the furfural hydrogenation reaction: Influence of the morphology of the silica support, Fuel. 319 (2022). https://doi.org/10.1016/j.fuel.2022.123827.
[30] L.W. Burnett, I.B. Johns, R.F. Holdren, R.M. Hixon, Production of 2-Methylfuran by Vapor-Phase Hydrogenation of Furfural, Ind. Eng. Chem. 40 (1948) 502–505. https://doi.org/10.1021/ie50459a034.
[31] C.P. Jiménez-Gómez, J.A. Cecilia, D. Durán-Martín, R. Moreno-Tost, J.

Santamaría-González, J. Mérida-Robles, R. Mariscal, P. Maireles-Torres, Gas-phase hydrogenation of furfural to furfuryl alcohol over Cu/ZnO catalysts, J. Catal. 336 (2016) 107–115. https://doi.org/10.1016/j.jcat.2016.01.012.
[32] F. Dong, Y.Y. Zhu, H. Zheng, Y.Y. Zhu, X. Li, Y. Li, Cr-free Cu-catalysts for the selective hydrogenation of biomass-derived furfural to 2-methylfuran: The synergistic effect of metal and acid sites, J. Mol. Catal. A Chem. 398 (2015) 140–148. https://doi.org/10.1016/j.molcata.2014.12.001.
[33] C.P. Jiménez-Gómez, J.A. Cecilia, F.I. Franco-Duro, M. Pozo, R. Moreno-Tost, P. Maireles-Torres, Promotion effect of Ce or Zn oxides for improving furfuryl alcohol yield in the furfural hydrogenation using inexpensive Cu-based catalysts, Mol. Catal. 455 (2018) 121–131. https://doi.org/10.1016/j.mcat.2018.06.001.
[34] A. Guerrero-Torres, C.P. Jiménez-Gómez, J.A. Cecilia, C. García-Sancho, J.J. Quirante-Sánchez, J.M. Mérida-Robles, P. Maireles-Torres, Influence of the incorporation of basic or amphoteric oxides on the performance of Cu-based catalysts supported on sepiolite in furfural hydrogenation, Catalysts. 9 (2019).
[35] J. Wu, Y. Shen, C. Liu, H. Wang, C. Geng, Z. Zhang, Vapor phase hydrogenation of furfural to furfuryl alcohol over environmentally friendly Cu-Ca/SiO2 catalyst, Catal. Commun. 6 (2005) 633–637. https://doi.org/10.1016/j.catcom.2005.06.009.
[36] B.M. Nagaraja, A.H. Padmasri, B. David Raju, K.S. Rama Rao, Vapor phase selective hydrogenation of furfural to furfuryl alcohol over Cu-MgO coprecipitated catalysts, J. Mol. Catal. A Chem. 265 (2007) 90–97. https://doi.org/10.1016/j.molcata.2006.09.037.
[37] Q. Hu, L. Yang, G. Fan, F. Li, Hydrogenation of biomass-derived compounds containing a carbonyl group over a copper-based nanocatalyst: Insight into the origin and influence of surface oxygen vacancies, J. Catal. 340 (2016) 184–195. https://doi.org/10.1016/j.jcat.2016.05.008.
[38] I. Ro, Y. Liu, M.R. Ball, D.H.K. Jackson, J.P. Chada, C. Sener, T.F. Kuech, R.J. Madon, G.W. Huber, J.A. Dumesic, Role of the Cu-ZrO2 Interfacial Sites for Conversion of Ethanol to Ethyl Acetate and Synthesis of Methanol from CO2 and H2, ACS Catal. 6 (2016) 7040–7050. https://doi.org/10.1021/acscatal.6b01805.
[39] L. Jiao, J.R. Regalbuto, The synthesis of highly dispersed noble and base metals on silica via strong electrostatic adsorption: I. Amorphous silica, J. Catal. 260 (2008) 329–341. https://doi.org/10.1016/j.jcat.2008.09.022.
[40] G.K. Williamson, W.H. Hall, X-ray line broadening from filed aluminium and wolfram, Acta Metall. 1 (1953) 22–31. https://doi.org/10.1016/0001-6160(53)90006-6.
[41] S. Brunauer, P.H. Emmett, E. Teller, Adsorption of Gases in Multimolecular Layers, J. Am. Chem. Soc. 60 (1938) 309–319. https://doi.org/10.1021/ja01269a023.
[42] J. Landers, G.Y. Gor, A. V. Neimark, Density functional theory methods for characterization of porous materials, Colloids Surfaces A Physicochem. Eng. Asp. 437 (2013) 3–32. https://doi.org/10.1016/j.colsurfa.2013.01.007.
[43] E.P. Barrett, L.G. Joyner, P.P. Halenda, The Determination of Pore Volume and Area Distributions in Porous Substances. I. Computations from Nitrogen Isotherms, J. Am. Chem. Soc. 73 (1951) 373–380. https://doi.org/10.1021/ja01145a126.
[44] M.J. Campos Molina, R. Mariscal, M. Ojeda, M. López Granados, Cyclopentyl methyl ether: A green co-solvent for the selective dehydration of lignocellulosic

pentoses to furfural, Bioresour. Technol. 126 (2012) 321–327. https://doi.org/10.1016/j.biortech.2012.09.049.
[45] C.P. Jiménez-Gómez, J.A. Cecilia, R. Moreno-Tost, P. Maireles-Torres, Selective Production of 2-Methylfuran by Gas-Phase Hydrogenation of Furfural on Copper Incorporated by Complexation in Mesoporous Silica Catalysts, ChemSusChem. 10 (2017) 1448.
[46] K. Peng, Y. Hou, Y. Zhang, X. Liu, Y. Li, B. Li, Z. Zeng, Z. Huang, Corrigendum to "Engineering oxygen vacancies in metal-doped MnO2 nanospheres for boosting the low-temperature toluene oxidation" [Fuel 314 (2022) 123123](S0016236121029823)(10.1016/j.fuel.2021.123123), Fuel. 321 (2022) 123965. https://doi.org/10.1016/j.fuel.2022.123965.
[47] M. Bouman, X. Qin, V. Doan, B.L.D. Groven, F. Zaera, Reaction of methylcyclopentadienyl manganese tricarbonyl on silicon oxide surfaces: Implications for thin film atomic layer depositions, Organometallics. 33 (2014) 5308–5315. https://doi.org/10.1021/om5006269.
[48] G. Koch, L. Schmack, T. Ressler, Tuning Size and Reducibility of Copper Oxide Particles Supported on SBA-15, ChemistrySelect. 1 (2016) 2040–2049. https://doi.org/10.1002/slct.201600428.
[49] J.A. Cecilia, A. Arango-Díaz, J. Marrero-Jerez, P. Núñez, E. Moretti, L. Storaro, E. Rodríguez-Castellón, Catalytic behaviour of CuO-CeO2 systems prepared by different synthetic methodologies in the CO-PROX reaction under CO2-H2O feed stream, Catalysts. 7 (2017) 1–20. https://doi.org/10.3390/catal7050160.
[50] M. Thommes, K. Kaneko, A. V. Neimark, J.P. Olivier, F. Rodriguez-Reinoso, J. Rouquerol, K.S.W. Sing, Physisorption of gases, with special reference to the evaluation of surface area and pore size distribution (IUPAC Technical Report), Pure Appl. Chem. 87 (2015) 1051–1069. https://doi.org/10.1515/pac-2014-1117.
[51] C. Sener, T.S. Wesley, A.C. Alba-Rubio, M.D. Kumbhalkar, S.H. Hakim, F.H. Ribeiro, J.T. Miller, J.A. Dumesic, PtMo Bimetallic Catalysts Synthesized by Controlled Surface Reactions for Water Gas Shift, ACS Catal. 6 (2016) 1334–1344. https://doi.org/10.1021/acscatal.5b02028.
[52] W.M.R. C.D. Wagner, J.F. Moulder, L.E. Davis, Handbook of X-Ray Photoelectron Spectroscopy, 1992.
[53] Q. Gan, H. He, K. Zhao, Z. He, S. Liu, Preparation of N-doped porous carbon coated MnO nanospheres through solvent-free in-situ growth of ZIF-8 on ZnMn2O4 for high-performance lithium-ion battery anodes, Electrochim. Acta. 266 (2018) 254–262. https://doi.org/10.1016/j.electacta.2018.02.010.
[54] Z. Yang, J. Lv, H. Pang, W. Yan, K. Qian, T. Guo, Z. Guo, Facile Synthesis of Coaxial CNTs/MnOx-Carbon Hybrid Nanofibers and Their Greatly Enhanced Lithium Storage Performance, Sci. Rep. 5 (2015) 1–10. https://doi.org/10.1038/srep17473.
[55] S. Sitthisa, T. Sooknoi, Y.G. Ma, P.B. Balbuena, D.E. Resasco, Kinetics and mechanism of hydrogenation of furfural on Cu/SiO_2 catalysts, J. Catal. 277 (2011) 1–13. https://doi.org/10.1016/j.jcat.2010.10.005.
[56] J. Lee, J.H. Seo, C. Nguyen-Huy, E. Yang, J.G. Lee, H. Lee, E.J. Jang, J.H. Kwak, J.H. Lee, H. Lee, K. An, Cu2O(100) surface as an active site for catalytic furfural hydrogenation, Appl. Catal. B Environ. 282 (2021) 119576. https://doi.org/10.1016/j.apcatb.2020.119576.
[57] C. Wen, Y. Cui, A. Yin, K. Fan, W.L. Dai, Remarkable Improvement of Catalytic Performance for a New Cobalt-Decorated Cu/HMS Catalyst in the Hydrogenation of Dimethyloxalate, ChemCatChem. 5 (2013) 138–141.

https://doi.org/10.1002/cctc.201200444.
[58] J. Gong, H. Yue, Y. Zhao, S. Zhao, L. Zhao, J. Lv, S. Wang, Synthesis of Ethanol via Syngas on Cu/SiO 2 Catalysts with Balanced Cu 0 − Cu + Sites, (2012) 1–4.
[59] H.G. Manyar, C. Paun, R. Pilus, D.W. Rooney, J.M. Thompson, C. Hardacre, Highly selective and efficient hydrogenation of carboxylic acids to alcohols using titania supported Pt catalysts w, (2010) 6279–6281. https://doi.org/10.1039/c0cc01365j.
[60] Y. Wang, D. Zhao, D. Rodríguez-Padrón, C. Len, Recent advances in catalytic hydrogenation of furfural, Catalysts. 9 (2019) 796.
[61] F. Wang, C. Li, X. Zhang, M. Wei, D.G. Evans, X. Duan, Catalytic behavior of supported Ru nanoparticles on the { 1 0 0 }, { 1 1 0 }, and { 1 1 1 } facet of CeO 2, J. Catal. 329 (2015) 177–186. https://doi.org/10.1016/j.jcat.2015.05.014.
[62] L.R. Baker, M. Van Spronsen, A. Hervier, X. Cai, S. Chen, L. Wang, G.A. Somorjai, Furfuraldehyde Hydrogenation on Titanium Oxide-Supported Platinum Nanoparticles Studied by Sum Frequency Generation Vibrational Spectroscopy : Acid − Base Catalysis Explains the Molecular Origin of Strong Metal − Support Interactions, (2012).

Table(Editable version)
Click here to access/download;Table(Editable version);Tables.docx

Table 1. Textural properties determined from the N_2 adsorption-desorption isotherms at -196 ºC of the Cu and 1Cu:0.15Mn catalysts supported on silica.

Sample	S_{BET} (m^2/g)	t-plot (m^2/g)	Pore volume (cm^3/g)	Micropore volume (cm^3/g)
Cu_{SEA}	175	21	0.530	0.007
$1Cu_{IMP}$:$0.15Mn_{IMP}$	188	16	0.540	0.004
$1Cu_{SEA}$:$0.15Mn_{IMP}$	169	19	0.526	0.006
$1Cu_{SEA}$:$0.15Mn_{CSR}$	155	31	0.524	0.012

Table 2. Spectral parameters obtained from XPS of the Cu and 1Cu:0.15Mn catalysts supported on silica.

Sample	Atomic concentrations (%)					Superficial molar ratio	
						Experimental	Theoretical
	C 1s	O 1s	Si 2p	Mn 2p	Cu 2p	Cu/Mn	Cu/Mn
Cu_{SEA}	6.78	60.98	30.60	-	1.88	∞	∞
$1Cu_{IMP}$:0.15Mn_{IMP}	5.75	61.38	31.03	1.19	0.65	0.55	6.67
$1Cu_{SEA}$:0.15Mn_{IMP}	9.55	59.29	28.22	1.36	1.58	1.36	6.67
$1Cu_{SEA}$:0.15Mn_{CSR}	9.03	58.36	30.15	0.67	1.79	2.67	6.67

Table 3. Spectral parameters obtained from XPS of the Cu and $1Cu_{SEA}$:zMn_{IMP} catalysts supported on silica.

Sample	Atomic concentrations (%)					Superficial molar ratio	
						Experimental	Theoretical
	C 1s	O 1s	Si 2p	Mn 2p	Cu 2p	Cu/Mn	Cu/Mn
Cu_{SEA}	6.78	60.98	30.60	-	1.88	∞	∞
$1Cu_{SEA}$:$0.15Mn_{IMP}$	9.55	59.29	28.22	1.36	1.58	1.36	6.67
$1Cu_{SEA}$:$0.30Mn_{IMP}$	10.22	56.68	28.24	3.23	1.63	0.50	3.33
$1Cu_{SEA}$:$0.45Mn_{IMP}$	4.10	60.56	30.82	3.40	1.11	0.32	2.22

Table 4. Textural properties determined from the N_2 adsorption-desorption isotherms at -196 ºC of the Cu and $1Cu_{SEA}$:zMn_{IMP} catalysts supported on silica.

Sample	S_{BET} (m^2/g)	t-plot (m^2/g)	Pore volume (cm^3/g)	Micropore volumen (cm^3/g)
Cu_{SEA}	175	21	0.530	0.007
$1Cu_{SEA}$:$0.15Mn_{IMP}$	169	19	0.526	0.006
$1Cu_{SEA}$:$0.30Mn_{IMP}$	162	24	0.491	0.008
$1Cu_{SEA}$:$0.45Mn_{IMP}$	177	8	0.516	0.003

Figure Click here to access/download;Figure;Figures.docx

List of captions

Figure 1. H_2-TPR profiles of the Cu and 1Cu:0.15Mn catalysts supported on silica.

Figure 2. X-ray diffractograms of the Cu and 1Cu:0.15Mn catalysts supported on silica.

Figure 3. TEM micrographs and EDX mapping of Cu_{SEA} (A), $1Cu_{IMP}$:$0.15Mn_{IMP}$ (B), $1Cu_{SEA}$:$0.15Mn_{IMP}$ (C), and $1Cu_{SEA}$:$0.15Mn_{CSR}$ (D). Scale bar: 60 nm.

Figure 4. N_2 adsorption-desorption isotherms at -196 ºC of the Cu and 1Cu:0.15Mn catalysts supported on silica.

Figure 5. Cu 2p core level spectra (A), Cu_{LMM} Auger line (B), and Mn 2p core level spectra (C) of the Cu and 1Cu:0.15Mn catalysts supported on silica.

Figure 6. FUR conversion (A), FOL yield (B), and MF yield (C) in the gas-phase FUR hydrogenation using Cu and 1Cu:0.15Mn catalysts supported on silica. Experimental conditions: mass of catalyst = 0.15 g, reaction temperature = 190 ºC, pressure = 0.1 MPa, H_2 flow = 10 mL min^{-1}, and feed flow = 2.3 mmol FUR h^{-1}.

Figure 7. FUR conversion (A), FOL yield (B), and MF yield (C) in the gas-phase FUR hydrogenation using Cu and $1Cu_{SEA}$:zMn_{IMP} catalysts supported on silica. Experimental conditions: mass of catalyst = 0.15 g, reaction temperature = 190 ºC, pressure = 0.1 MPa, H_2 flow = 10 mL min^{-1}, and feed flow = 2.3 mmol FUR h^{-1}.

Figure 8. H_2-TPR profiles of the Cu and $1Cu_{SEA}$:zMn_{IMP} catalysts supported on silica.

Figure 9. X-ray diffractograms of the Cu and $1Cu_{SEA}$:zMn_{IMP} catalysts supported on silica.

Figure 10. TEM micrographs and EDX mapping of Cu_{SEA} (A), $1Cu_{SEA}$:$0.15Mn_{IMP}$ (B), $1Cu_{SEA}$:$0.30Mn_{IMP}$ (C), and $1Cu_{SEA}$:$0.45Mn_{IMP}$ (D). Scale: 60 nm.

Figure 11. Cu_{LMM} Auger line (A) and Mn 2p core level spectra (B) of the Cu and $1Cu_{SEA}$:zMn_{IMP} catalysts supported on silica.

Figure 12. FUR conversion (A), FOL yield (B), and MF yield (C) in the gas-phase FUR hydrogenation using Cu and 1Cu:0.15Mn catalysts supported on silica. Experimental conditions: mass of catalyst = 0.15 g, reaction temperature = 190 ºC, reaction time = 24 h, pressure = 0.1 MPa, H_2 flow = 10 mL min^{-1}, and feed flow = 2.3 mmol FUR h^{-1}.

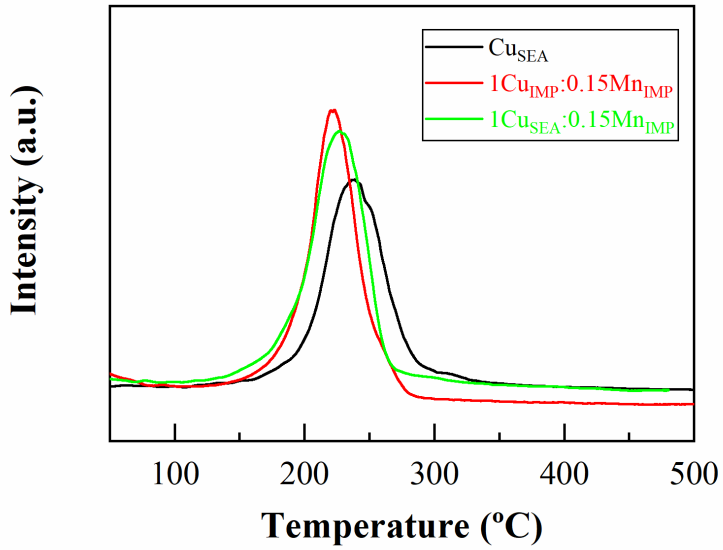
Cu$_{SEA}$
1Cu$_{IMP}$:0.15Mn$_{IMP}$
1Cu$_{SEA}$:0.15Mn$_{IMP}$
Intensity (a.u.)
100
200
300
400
500
Temperature (ºC)

Figure 1

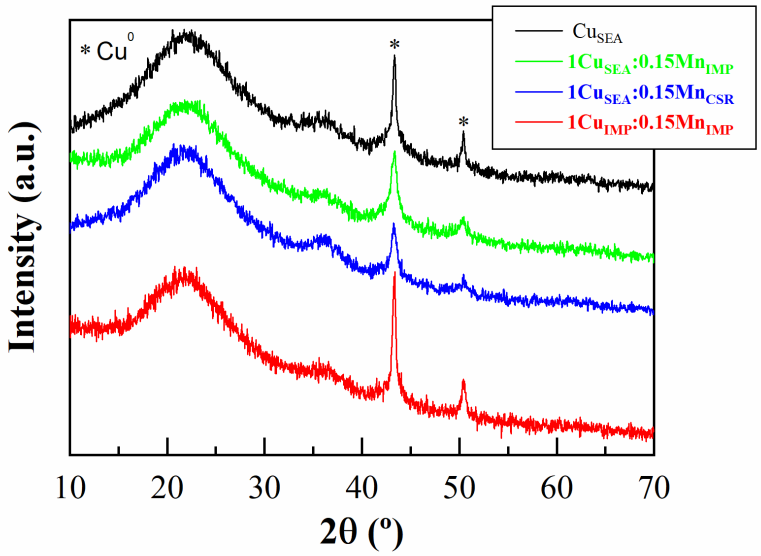
* Cu0
*
*
Cu_SEA
1Cu_SEA:0.15Mn_IMP
1Cu_SEA:0.15Mn_CSR
1Cu_IMP:0.15Mn_IMP
Intensity (a.u.)
10
20
30
40
50
60
70
2θ (º)

Figure 2

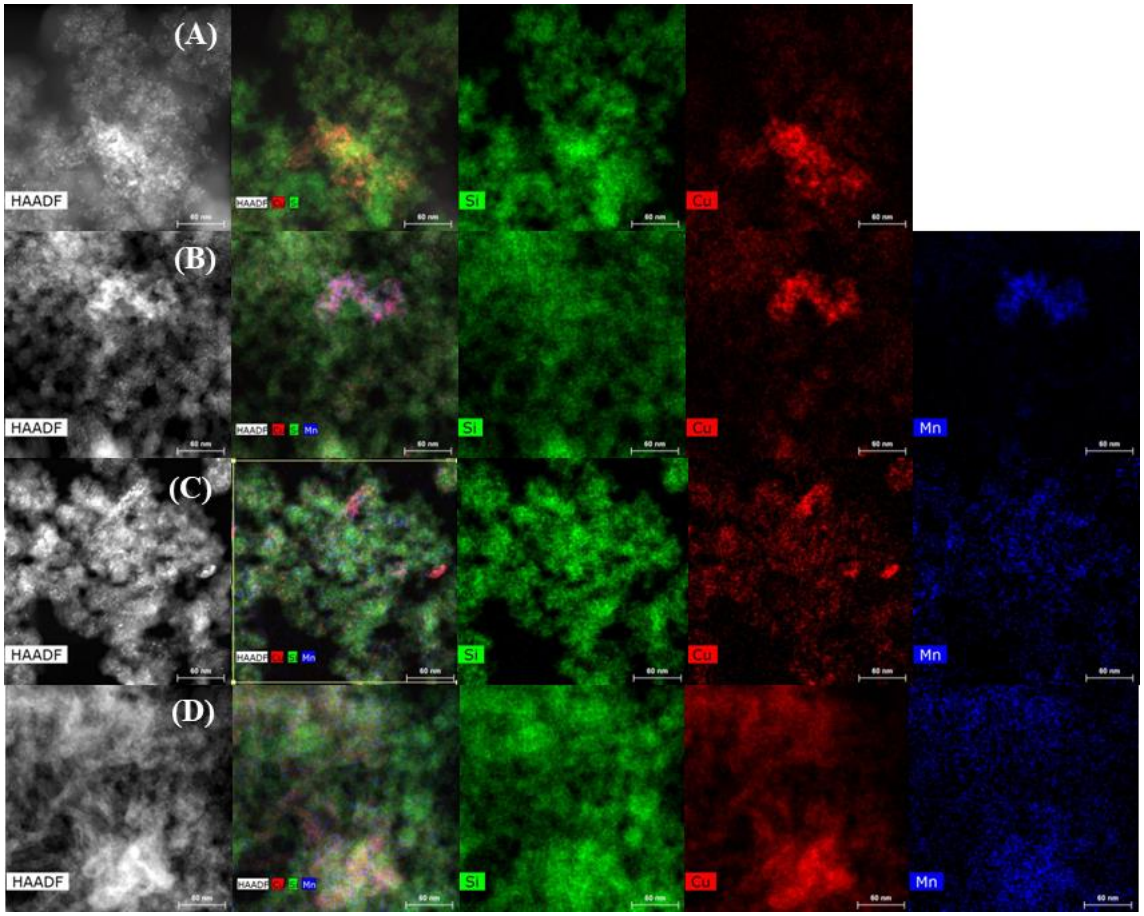

Figure 3

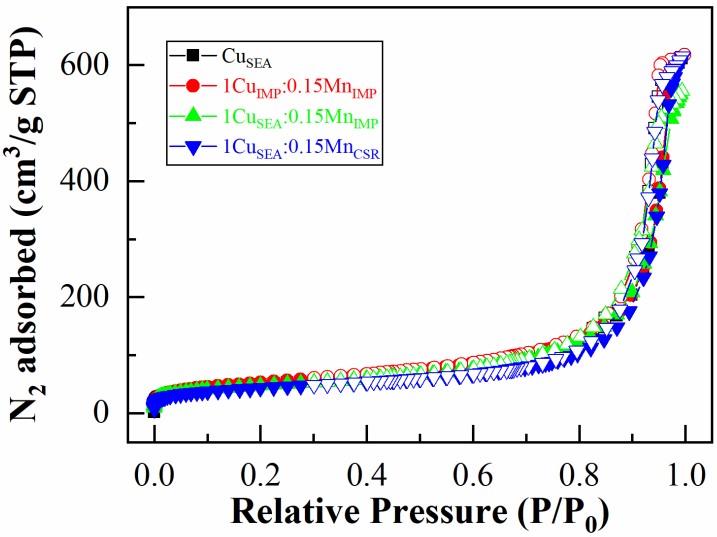
Cu_SEA
1Cu_IMP:0.15Mn_IMP
1Cu_SEA:0.15Mn_IMP
1Cu_SEA:0.15Mn_CSR
N2 adsorbed (cm3/g STP)
600
400
200
0
0.0
0.2
0.4
0.6
0.8
1.0
Relative Pressure (P/P0)

Figure 4

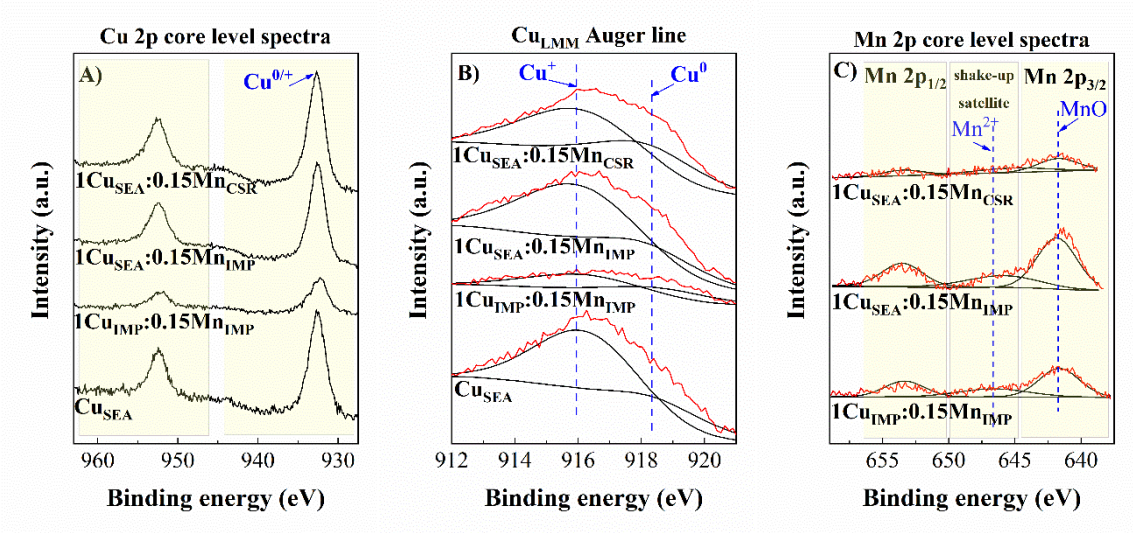
Cu 2p core level spectra
A)
Cu0/+
1CuSEA:0.15MnCSR
1CuSEA:0.15MnIMP
1CuIMP:0.15MnIMP
CuSEA
Intensity (a.u.)
960
950
940
930
Binding energy (eV)
CuLMM Auger line
B)
Cu+
Cu0
1CuSEA:0.15MnCSR
1CuSEA:0.15MnIMP
1CuIMP:0.15MnIMP
CuSEA
Intensity (a.u.)
912
914
916
918
920
Binding energy (eV)
Mn 2p core level spectra
C)
Mn 2p1/2
shake-up
satellite
Mn 2p3/2
MnO
Mn2+
1CuSEA:0.15MnCSR
1CuSEA:0.15MnIMP
1CuIMP:0.15MnIMP
Intensity (a.u.)
655
650
645
640
Binding energy (eV)

Figure 5

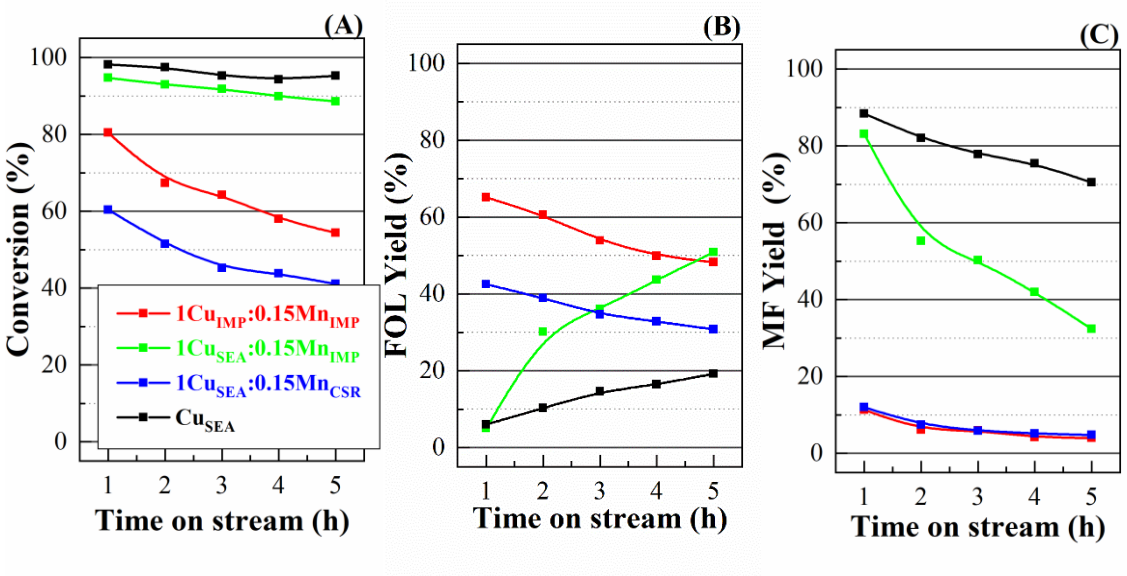
(A)
Conversion (%)
Time on stream (h)
1Cu$_{IMP}$:0.15Mn$_{IMP}$
1Cu$_{SEA}$:0.15Mn$_{IMP}$
1Cu$_{SEA}$:0.15Mn$_{CSR}$
Cu$_{SEA}$
(B)
FOL Yield (%)
Time on stream (h)
(C)
MF Yield (%)
Time on stream (h)

Figure 6

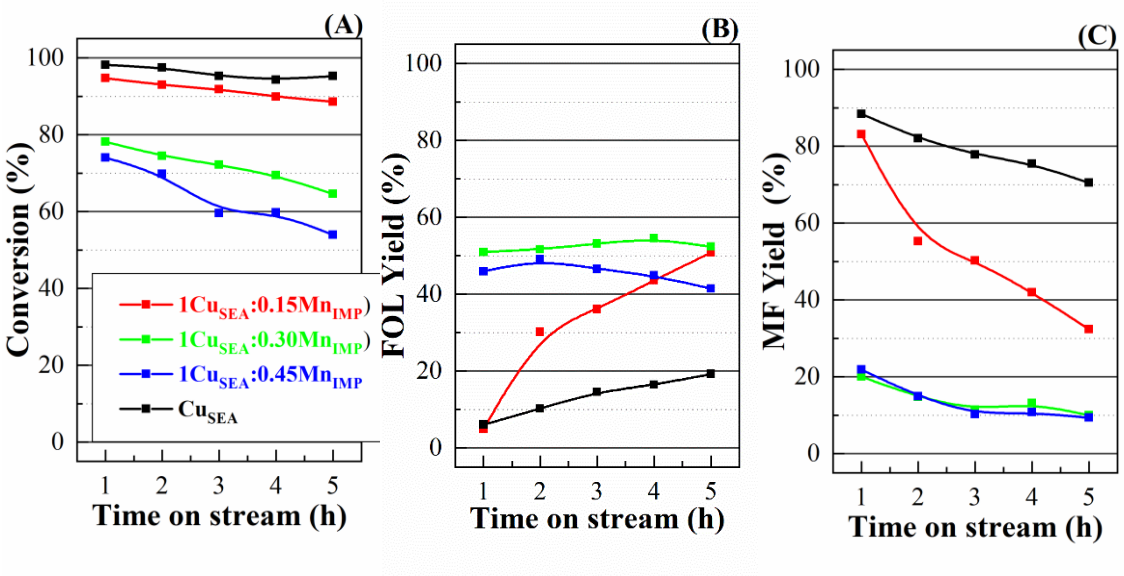
(A)
Conversion (%)
Time on stream (h)
1Cu$_{SEA}$:0.15Mn$_{IMP}$)
1Cu$_{SEA}$:0.30Mn$_{IMP}$)
1Cu$_{SEA}$:0.45Mn$_{IMP}$
Cu$_{SEA}$
(B)
FOL Yield (%)
Time on stream (h)
(C)
MF Yield (%)
Time on stream (h)

Figure 7

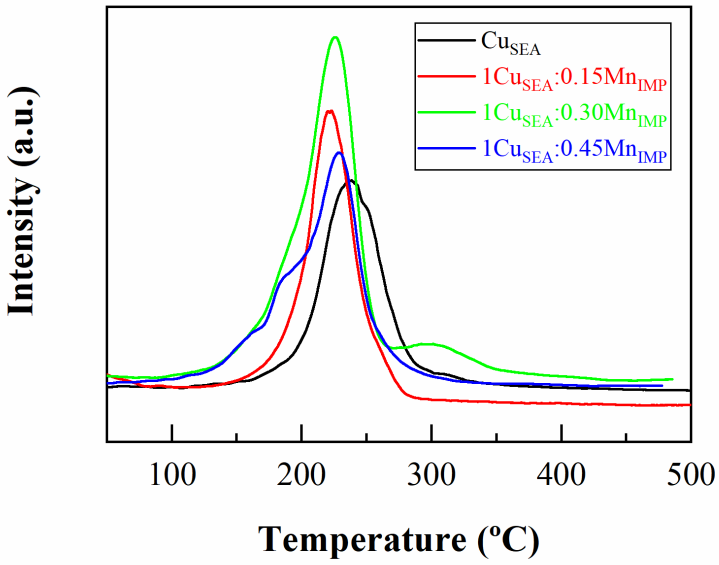
Cu$_{SEA}$
1Cu$_{SEA}$:0.15Mn$_{IMP}$
1Cu$_{SEA}$:0.30Mn$_{IMP}$
1Cu$_{SEA}$:0.45Mn$_{IMP}$
Intensity (a.u.)
100
200
300
400
500
Temperature (ºC)

Figure 8

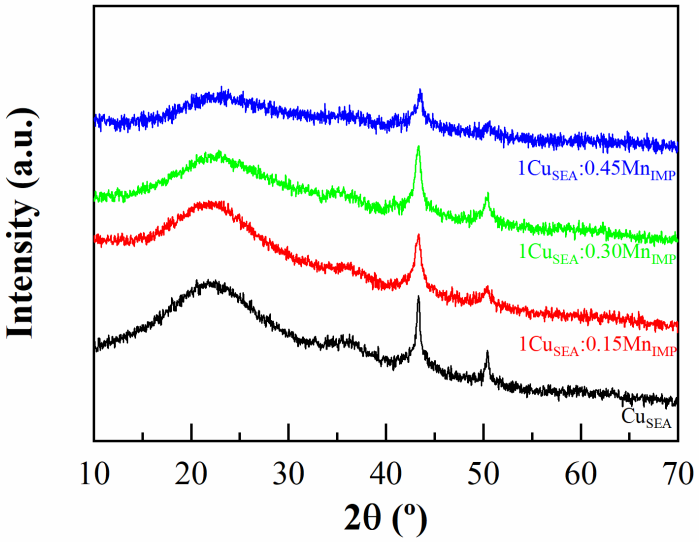
Intensity (a.u.)
1Cu$_{SEA}$:0.45Mn$_{IMP}$
1Cu$_{SEA}$:0.30Mn$_{IMP}$
1Cu$_{SEA}$:0.15Mn$_{IMP}$
Cu$_{SEA}$
10
20
30
40
50
60
70
2θ (º)

Figure 9

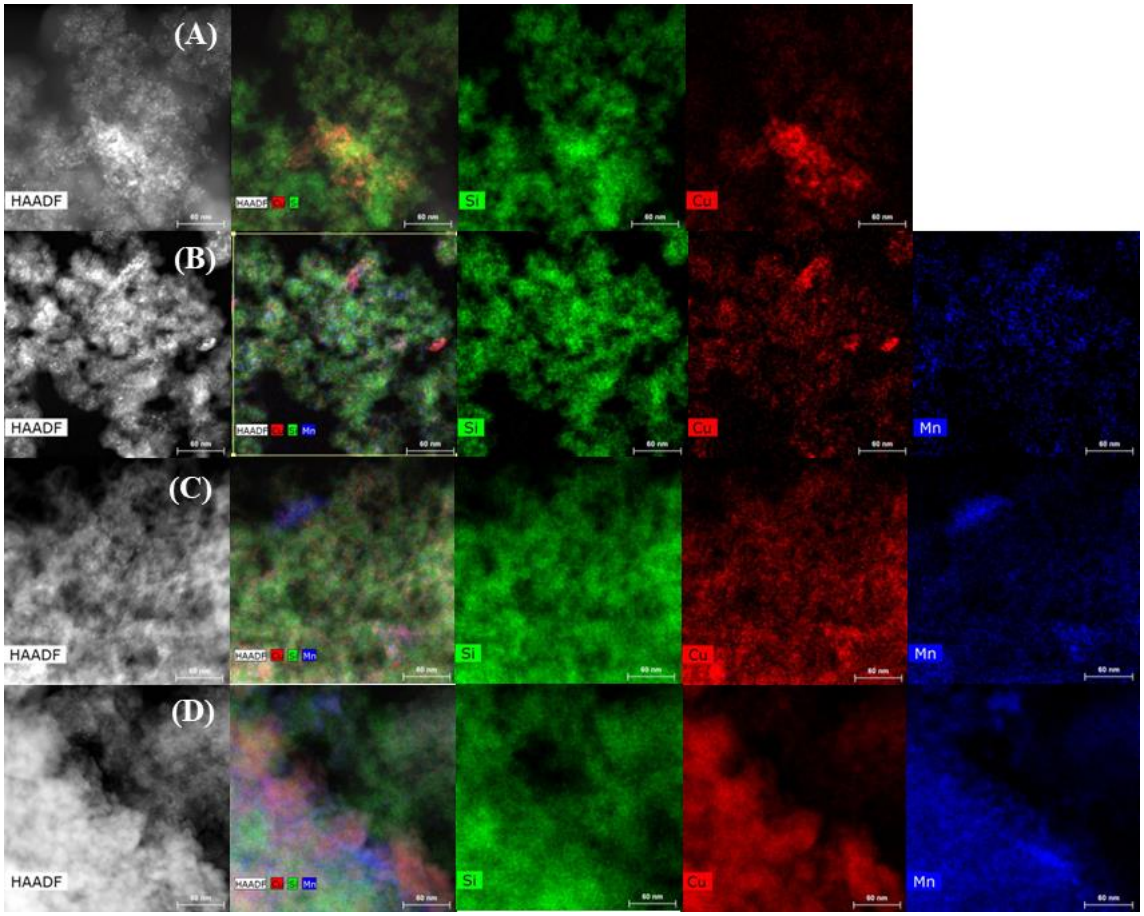

Figure 10

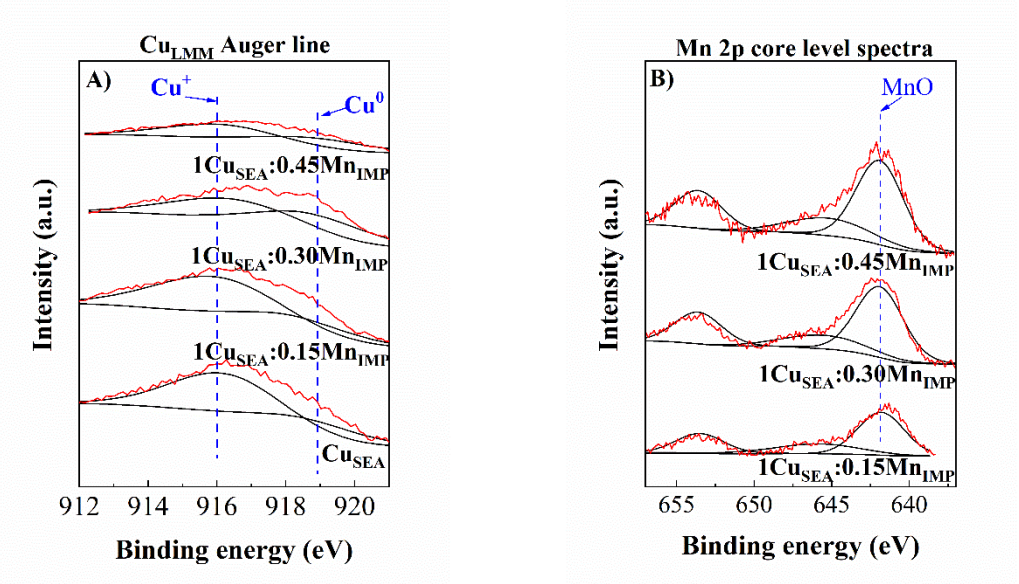
Cu_LMM Auger line
A)
Cu+
Cu0
1Cu_SEA:0.45Mn_IMP
1Cu_SEA:0.30Mn_IMP
1Cu_SEA:0.15Mn_IMP
Cu_SEA
Intensity (a.u.)
912
914
916
918
920
Binding energy (eV)
Mn 2p core level spectra
B)
MnO
1Cu_SEA:0.45Mn_IMP
1Cu_SEA:0.30Mn_IMP
1Cu_SEA:0.15Mn_IMP
Intensity (a.u.)
655
650
645
640
Binding energy (eV)

Figure 11

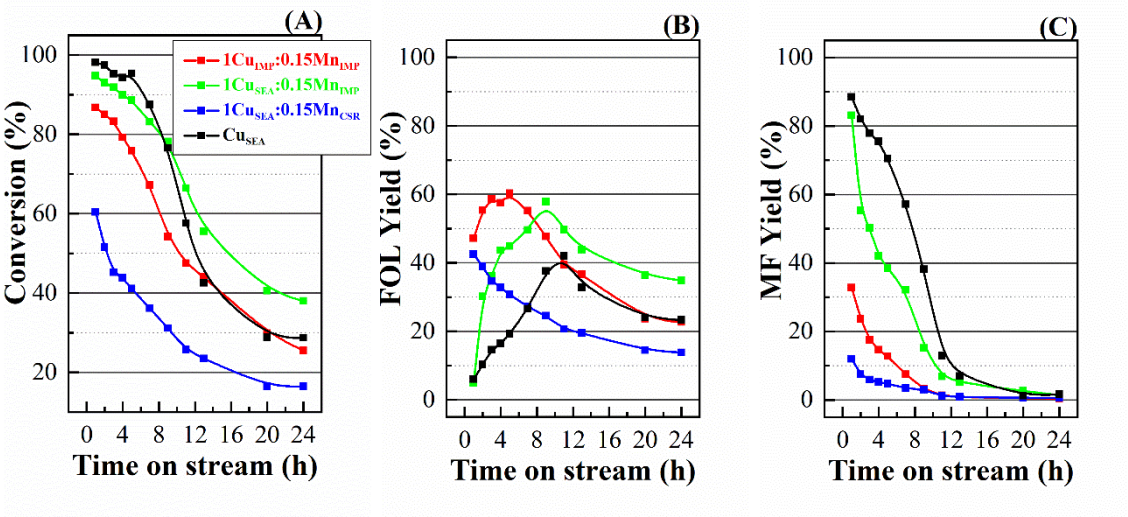
(A)
(B)
(C)
Conversion (%)
FOL Yield (%)
MF Yield (%)
Time on stream (h)
1Cu$_{IMP}$:0.15Mn$_{IMP}$
1Cu$_{SEA}$:0.15Mn$_{IMP}$
1Cu$_{SEA}$:0.15Mn$_{CSR}$
Cu$_{SEA}$

Figure 12